Article:
Stjern, CW, Forster, PM, Jia, H et al. (2023) The Time Scales of Climate Responses to Carbon Dioxide and Aerosols. Journal of Climate, 36 (11). pp. 3537-3551. ISSN: 0894-8755

https://doi.org/10.1175/jcli-d-22-0513.1

The Time Scales of Climate Responses to Carbon Dioxide and Aerosols

CAMILLA W. STJERN,[a] PIERS M. FORSTER,[b] HAILING JIA,[c] CAROLINE JOUAN,[a] MATTHEW R. KASOAR,[d] GUNNAR MYHRE,[a] DIRK OLIVIÉ,[e] JOHANNES QUAAS,[c] BJØRN H. SAMSET,[a] MARIA SAND,[a] TOSHIHIRO TAKEMURA,[f] APOSTOLOS VOULGARAKIS,[f,g] AND CHRISTOPHER D. WELLS[b,d]

[a] *CICERO Center for International Climate Research, Oslo, Norway*
[b] *University of Leeds, Leeds, United Kingdom*
[c] *Universität Leipzig, Leipzig, Germany*
[d] *Imperial College London, London, United Kingdom*
[e] *Norwegian Meteorological Institute, Oslo, Norway*
[f] *Kyushu University, Fukuoka, Japan*
[g] *Technical University of Crete, Chania, Greece*

(Manuscript received 30 July 2022, in final form 11 January 2023)

ABSTRACT: The climate system responds to changes in the amount of atmospheric greenhouse gases or aerosols through rapid processes, triggered within hours and days, and through slower processes, where the full response may only be seen after centuries. In this paper, we aim to elucidate the mechanisms operating on time scales of hours to years to better understand the response of key climate quantities such as energy fluxes, temperature, and precipitation after a sudden increase in either carbon dioxide (CO_2), black carbon (BC), or sulfate (SO_4) aerosols. The results are based on idealized simulations from six global climate models. We find that the effect of changing ocean temperatures kicks in after a couple of months. Rapid precipitation reductions start occurring instantly and are established after just a few days. For BC, they constitute most of the equilibrium response. For CO_2 and SO_4, the magnitude of the precipitation response gradually increases as surface warming/cooling evolves, and for CO_2, the sign of the response changes from negative to positive after 2 years. Rapid cloud adjustments are typically established within the first 24 h, and while the magnitude of cloud feedbacks for CO_2 and SO_4 increases over time, the geographical pattern of the equilibrium cloud change is present already after the first year. While there are model differences, our work underscores the overall similarity of the major time-varying processes and responses simulated by current global models and hence the robustness of key features of simulated responses to historical and future anthropogenic forcing.

SIGNIFICANCE STATEMENT: How does the climate system respond to a change in the amount of atmospheric greenhouse gases or aerosols? Some processes are rapid, responding within hours and days. Others are slow, and the full response to a forcing of the climate may only be seen after centuries. In this paper, we use six global climate models to investigate the time scales of climate responses to carbon dioxide, black carbon, and sulfate, focusing on key climate quantities, such as temperature, precipitation, and clouds. While there are ample model differences, our work underscores the overall similarity of the major time-varying processes and responses simulated by current global models and hence the robustness of key features of simulated responses to historical and future anthropogenic forcing.

KEYWORDS: Atmosphere; Aerosols; Climate change; Clouds; Climate models

1. Introduction

The climate system responds to a climate forcing, such as an increase in greenhouse gases or aerosols, on a range of different time scales. Instant radiative responses trigger fast adjustments in a variety of atmospheric variables (Sherwood et al. 2015), eventually accompanied by the slower feedbacks mediated by a change in ocean temperatures. The 2013 report from the Intergovernmental Panel on Climate Change (IPCC) reflected an emerging consensus in the literature that a metric describing the climate impact of a forcing agent (i.e., radiative forcing) should contain not only the instantaneous radiative effect and stratospheric temperature adjustment but all responses that are independent of surface temperature change (Boucher et al. 2013; Myhre et al. 2013). Hence, rapid adjustments—the tropospheric climate responses that occur before surface temperatures start changing—were included in the new metric "effective radiative forcing" (ERF). This shift was motivated by a growing amount of evidence that the rapid adjustments could constitute a substantial part of the total climate effect (Hansen et al. 2005; Lohmann et al. 2010) and that not only aerosols but also long-lived greenhouse gases trigger such responses. The ERF also linked more closely to the final

Denotes content that is immediately available upon publication as open access.

Supplemental information related to this paper is available at the Journals Online website: https://doi.org/10.1175/JCLI-D-22-0513.s1.

Corresponding author: Camilla W. Stjern, camilla.stjern@cicero.oslo.no

DOI: 10.1175/JCLI-D-22-0513.1

surface temperature change than the traditional (instantaneous or stratosphere-adjusted) radiative forcing (Richardson et al. 2019).

Distinction between adjustments and feedbacks is not straightforward. While the nomenclature indicates a temporal aspect, the rapid adjustments (like the feedbacks) are not defined by their time dependency but rather distinguished by the type of mechanism driving them (surface temperature change or not; Forster et al. 2021). Although they typically occur on time scales of seasons or less (Myhre et al. 2013), and mostly within a few days of applying the forcing (Dong et al. 2009), some rapid adjustments (e.g., within the cryosphere or biosphere) can take years. Studying the time scales of responses to a forcing agent can give valuable insight into the physical mechanisms involved. Improved knowledge on the timing of different climate responses, regardless of whether labeled adjustments or feedbacks, can prove useful for developing informed mitigation strategies. A better understanding of rapid adjustments is also imperative to understanding model spread in estimates of the equilibrium climate sensitivity (Andrews et al. 2009; Forster et al. 2021; Zelinka et al. 2013).

The IPCC Sixth Assessment Report (AR6; Forster et al. 2021) quantifies rapid adjustments and assesses recent literature. An important finding is that the magnitude of the rapid responses shows a strong dependency on the forcing agent (Smith et al. 2020; Samset et al. 2016; Kvalevåg et al. 2013; Andrews et al. 2010). How quickly the full climate response is realized therefore depends on the climate driver and the extent to which it triggers processes that operate on fast or slow time scales. For instance, rapid adjustments to perturbations in greenhouse gases make up a substantial part of the total long-term effect (Kamae et al. 2015), and perturbations in absorbing aerosols may even dominate the total response (Samset et al. 2016). For scattering aerosols, however, the main responses occur on longer time scales.

Several studies exist that show the temporal evolution of climate responses to carbon dioxide (CO_2; Kamae et al. 2015; Wang and Huang 2020; Kamae and Watanabe 2013; Dong et al. 2009; Bony et al. 2013; Cao et al. 2012) and aerosols (Tian et al. 2017; Hansen et al. 1997; Rotstayn et al. 2015). However, the more detailed analyses tend to be single-model studies of CO_2 responses only, while those comparing several models and/or climate drivers do not show the earliest (first hours and days) responses. In this paper, we follow the evolution of atmospheric responses to instantaneous perturbations in CO_2 and aerosols—from the immediate radiative response through the stratospheric and tropospheric adjustments of the first hours and days, the slower rapid adjustments over the following weeks and months, and finally the feedback response up to year 100. Comparable experiments are conducted with six different global climate models. As individual models may have differing levels of realism in their representation of processes related to rapid responses, quantification of responses using multiple models is a valuable analytical tool.

The next section gives an overview of models and methods. Section 3 starts with an account of near-surface air temperature and precipitation responses. We then show how CO_2, black carbon (BC), and sulfate (SO_4) influence the evolution of radiative fluxes over the first hours, days, months, and years after perturbation. In the remaining subsections, we demonstrate how these radiative flux changes are linked to the temporal evolution of atmospheric heating rates, temperature, precipitation, and clouds. Findings are summarized in section 4.

2. Methods

Analyses are based on a combination of simulated data with a range of different temporal resolutions. Hourly data were obtained from simulations performed by 6 models [CESM1(CAM4), HadGEM3-GA4, NorESM1-M, GISS-E2.1, MIROC-SPRINTARS, and ICON-HAM; see Table S1 in the online supplemental material]. Models performed a baseline simulation (BASE) using year 2000 emission levels and CO_2 concentrations. Important radiative and meteorological variables were stored on an hourly basis. To isolate the atmospheric response to the perturbations, models were set up with fixed sea surface temperatures (fixed-SST). Note, however, that because most climate models are not able to hold land surface temperatures fixed, the land surfaces are allowed to cool/warm in these runs. After a spinup time of 4 years, simulations were run for 30 days (720 h), starting in the months of January, April, July, and October to take into account seasonal variation in the responses. Each of these simulations were then repeated twice with different meteorological starting conditions (using meteorological input from different years), resulting in a 3-member ensemble for each monthly starting point and thus a total of 12 ensemble members for each model. The perturbation experiments were branched off from the baseline run, having identical initial conditions as BASE. The climate response to greenhouse gases was represented by an experiment where CO_2 concentrations were instantly doubled (experiment CO2x2). To investigate responses to absorbing and scattering aerosols, experiments with a tenfold increase in anthropogenic BC and a fivefold increase in anthropogenic SO_4 were performed separately (experiments BCx10 and SO4x5, respectively). For these experiments, MIROC-SPRINTARS and ICON-HAM simulations were performed with perturbed aerosol emissions, while in the other models, aerosol concentrations were perturbed. This naturally induces additional intermodel differences in the timing of the responses to the aerosol experiments, as will be shown.

Daily, monthly, and yearly mean climate responses extending beyond the 30 days of the hourly simulations were analyzed by use of data from Precipitation Driver and Response Multimodel Intercomparison Project (PDRMIP; Myhre et al. 2017). In PDRMIP, experiments with the same perturbations as described above were performed by 10 global climate models, including five of the six models included in this study (all except ICON-HAM). Figures extending beyond the time scale of 1 month will thus be averages of these five models for consistency of responses between hourly and longer time scales. The PDRMIP experiments were performed both in

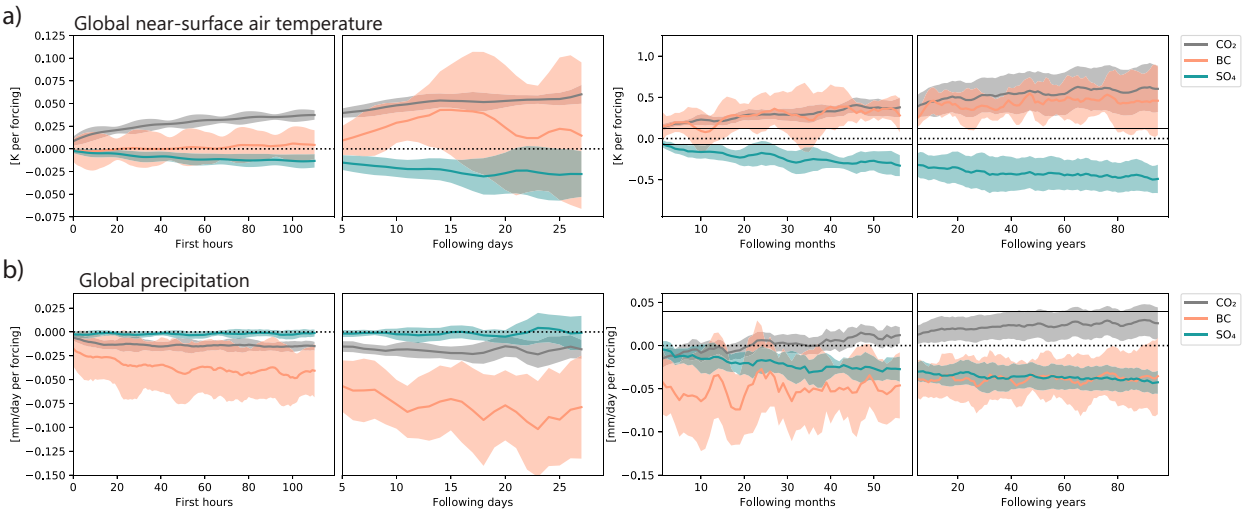

FIG. 1. (a) Evolution of global-mean temperature changes due to perturbations of CO_2, BC, and SO_4 for the initial hours and days (fixed-SST) and for the following months and years (coupled). Thin horizontal lines in the monthly and yearly panels mark the vertical limits of the hourly and daily panels, respectively. (b) As in (a), but for evolution of precipitation. All values are normalized by the absolute value of the ERF for the given model and experiment and show temperature and precipitation changes per W m^{-2} forcing. Lines are for the multimodel ensemble average; the shading shows the multimodel spread (intermodel standard deviation).

100-yr fully coupled model setups (later "coupled") where the atmosphere models are coupled to ocean and cryosphere models and also in 15-yr fixed-SST setups. While Forster et al. (2016) ideally recommend fixed-SST simulation lengths to be 30 years, most of the full adjustment will be realized by year 15. Comparing the time evolution of coupled versus fixed-SST climate responses allows us to investigate when the effect of increasing or decreasing ocean temperatures starts influencing the climate. ERF is calculated based on the fixed-SST experiments (averaging years 6–15) as the change in net radiative longwave plus shortwave flux at the top of atmosphere (Forster et al. 2016).

3. Results and discussion

We start, in Fig. 1, by presenting the evolution of the global-mean responses in near-surface air temperature and precipitation to the three climate driver perturbations. In the following subsections, we will take a closer look at the nature and timing of the processes behind these changes. While regional responses in particular to the geographically heterogeneous aerosol emission changes can be substantial and are particularly important on shorter time scales (Bellouin et al. 2016; Stjern et al. 2016; Williams et al. 2022; Samset et al. 2019), the present study focuses on the evolution of global means in order to show the overall responses and their time scales.

Figure 1a shows the temporal evolution of the ensemble- and model-average change in temperature for the three experiments CO2x2, BCx10, and SO4x5 relative to BASE. The shaded area indicates the intermodel spread in terms of plus and minus one standard deviation. For comparability between perturbations, each simulation is normalized by the magnitude of its ERF (see Table S2 for ERF values for each model and experiment). A nonnormalized version of Fig. 1 can be found in Fig. S1, while the temperature evolution (corresponding to Fig. 1a) for the individual models is given in Fig. S2. The first two panels of Fig. 1a are based solely on hourly data and show changes for the first 120 h (5 days) and for the subsequent 25 days, where hourly data are aggregated into daily mean values.

CO_2 causes a rapid increase in temperature (normalized by global-mean forcing) initially twice the magnitude of the response to SO_4, for which the temperature reduction is more gradual. The temperature response from BC remains statistically indistinguishable from zero for the first 5 days or so. Relative to the magnitude of the forcing, the model spread in the temperature response is small for CO_2 and SO_4 but larger and even crossing the zero line for BC (Fig. 1a). For BC, the spread in ERF-normalized temperature changes is substantially larger than in the nonnormalized version in Fig. S1 due to a combination of relatively large model spread and small ERF values (Table S2).

After about 15 days, there is an increase in model spread as well as an apparent break in the initial temperature change evolution; this signifies the onset of internal variability and can be seen for all three drivers. Up until this point, the memory of the atmosphere system contributes to clear signals. This is consistent with the results presented by Dong et al. (2009), who found in a single-model experiment with several ensemble members that after a little over 2 weeks following a doubling of CO_2 the internal variability becomes decorrelated and the ensemble members start deviating substantially (see also Deser et al. 2012).

The next two panels in Fig. 1a are based on monthly mean data; the first shows temperature changes from the second month and over the next 5 years, while in the last panel, we have aggregated monthly changes into yearly means and

show temperature changes up to year 100. Note the change in *y*-axis limits from daily to monthly time scales. We do not expect the ending of the first month of hourly data to line up perfectly with the beginning of the monthly mean time series because the latter always starts in February, while the hourly data are aggregates of all models, all ensemble members, and the four monthly startup points (see section 2).

After a little over six months, the slower SO_4-induced temperature change becomes comparable in magnitude to that from CO_2. A seasonal cycle is seen for the response to aerosols (SO_4 and BC) that are predominantly located in the Northern Hemisphere; CO_2 shows only a very muted seasonal cycle. Relative to the warming after 100 years of simulation, the impact of the BC perturbation has realized 90% of its final 0.4 K warming (per 1 W m^{-2} forcing) after about a decade. Correspondingly, 90% of the CO_2-driven warming [0.6 (W m^{-2})$^{-1}$] is established after slightly less than two decades, while the SO_4-driven cooling, which asymptotically approaches −0.5 K (W m^{-2})$^{-1}$, is established after about two decades.

The magnitude of the temperature change per forcing corresponds to the magnitude of the climate driver's efficacy. Note that in the first hours of the simulation, the efficacy of CO_2 is significantly stronger than that of both BC and SO_4 [e.g., around 0.025 K (W m^{-2})$^{-1}$ versus close to 0 K (W m^{-2})$^{-1}$ for BC and around 0.008 K (W m^{-2})$^{-1}$ for SO_4]. However, already from the second month of simulation the efficacies of the three drivers are statistically indistinguishable.

Finally, Fig. 1b shows global-mean precipitation changes for the three experiments. We will discuss precipitation changes in more detail in section 3a, but we note for now that the rapid precipitation response of the first few months is a precipitation reduction for all three climate drivers in spite of their widely differing impacts on temperature. For instance, BC immediately causes a stronger precipitation reduction than CO_2, despite a near-zero temperature response, while SO_4 causes a very weak precipitation response initially. Figure S3, which shows precipitation changes for the individual models, demonstrates that in the two models (ICON-HAM and MIROC-SPRINTARS) that perturbed emissions instead of concentrations, the rapid precipitation response to BC is slower. This is expected, as in these models, the aerosols will take time to propagate upward in the atmosphere, where their absorption efficiency and thus their potential to influence precipitation is higher (Samset and Myhre 2011). In the longer term (after 12–25 months, depending on model), the CO_2 precipitation response (Fig. 1c) turns positive and the (negative) response to SO_4 ends up as strong as the BC response. Note again the onset of strong day-to-day variability after about 2 weeks, and that, for instance, the peak in SO_4 precipitation change around day 24 can be attributed to this variability.

The very first changes in temperature and precipitation—observed in the first panels of Fig. 1—are triggered by radiative changes (Allen and Ingram 2002; Bony et al. 2013; Salzmann 2016). In the following subsections, we first take a look at the evolution of the atmospheric energy fluxes, how these influence atmospheric heating rates, and ultimately the response of temperature and clouds.

a. The evolution of the atmospheric energy fluxes

In Fig. 2, we show the temporal evolution of the atmospheric part of the shortwave (SW), longwave (LW), sensible heat (SH), and latent heat (LH) fluxes, starting with the very first hours and days, the following months, and all the way up to 100 years after simulation start (the latter two from the coupled simulations). Atmospheric (ATM) fluxes are calculated as the difference between fluxes at the surface (SRF) and the top of atmosphere (TOA). The focus on the atmospheric part of the fluxes in this figure is motivated by the fact that atmospheric absorption is such an important driver of the rapid responses (in particular precipitation) in the first hours after perturbation. To provide a fuller picture, however, TOA fluxes are shown in Fig. S4, and in narrow panels in Fig. 2 we also provide the total radiative imbalance (the sum of the four flux terms) within the atmosphere as well as at TOA and SRF. For simplicity, we here show absolute flux changes, not per-unit forcing.

An increase in the atmospheric LW flux follows immediately after the instantaneous increase in CO_2 due to the additional absorption of CO_2 (Fig. 2a). Thereafter, less LW radiation is sent out from (and thus remains within) the atmosphere due to a strong stratospheric reduction in the LW heating rate (the net, LW, and SW heating rates are shown in Fig. 3 and will be discussed further in section 3b). This reduction is compensated by enhanced LW radiation emitted by the troposphere due to an increase in temperature [see, e.g., Myhre et al. (2018), who show that these two effects are equal in magnitude but opposite in sign]. Shortwave absorption by CO_2 in the stratosphere produces a small positive SW flux. The physiological plant response to increased CO_2, in which plant stomata openings become narrower and surface evaporation (and associated surface cooling) is reduced (Park et al. 2021; Doutriaux-Boucher et al. 2009), is likely also playing a role. The stomata effect is, however, not included in all GCMs considered here, and a dedicated set of experiments would be needed to quantify its role in the flux changes these first hours. Over ocean surfaces, the reduced convection causes an increase in boundary layer moisture that further lowers evaporation over the ocean (Kamae and Watanabe 2013).

The LH flux continues to decrease over the first hours, in line with a gradual increase in atmospheric stability as the lower troposphere warms more than the surface temperature (temperature changes are shown in Fig. 4 and are more thoroughly discussed in section 3c). This strengthened stability weakens convection, and the combined effect of reduced humidity and increased stability reduces precipitation (O'Gorman et al. 2012), as seen in Fig. 1c. We find that precipitation changes are by far strongest in the tropics in the first hours and propagate poleward (Fig. S5). Kamae and Watanabe (2013) also found that CO_2-driven precipitation reduction over the ocean is larger over the tropical convective regions than over the subtropics in the first days, but this pattern was no longer visible in the long-term response. Here, we confirm that this is a common precipitation response pattern for all three climate drivers.

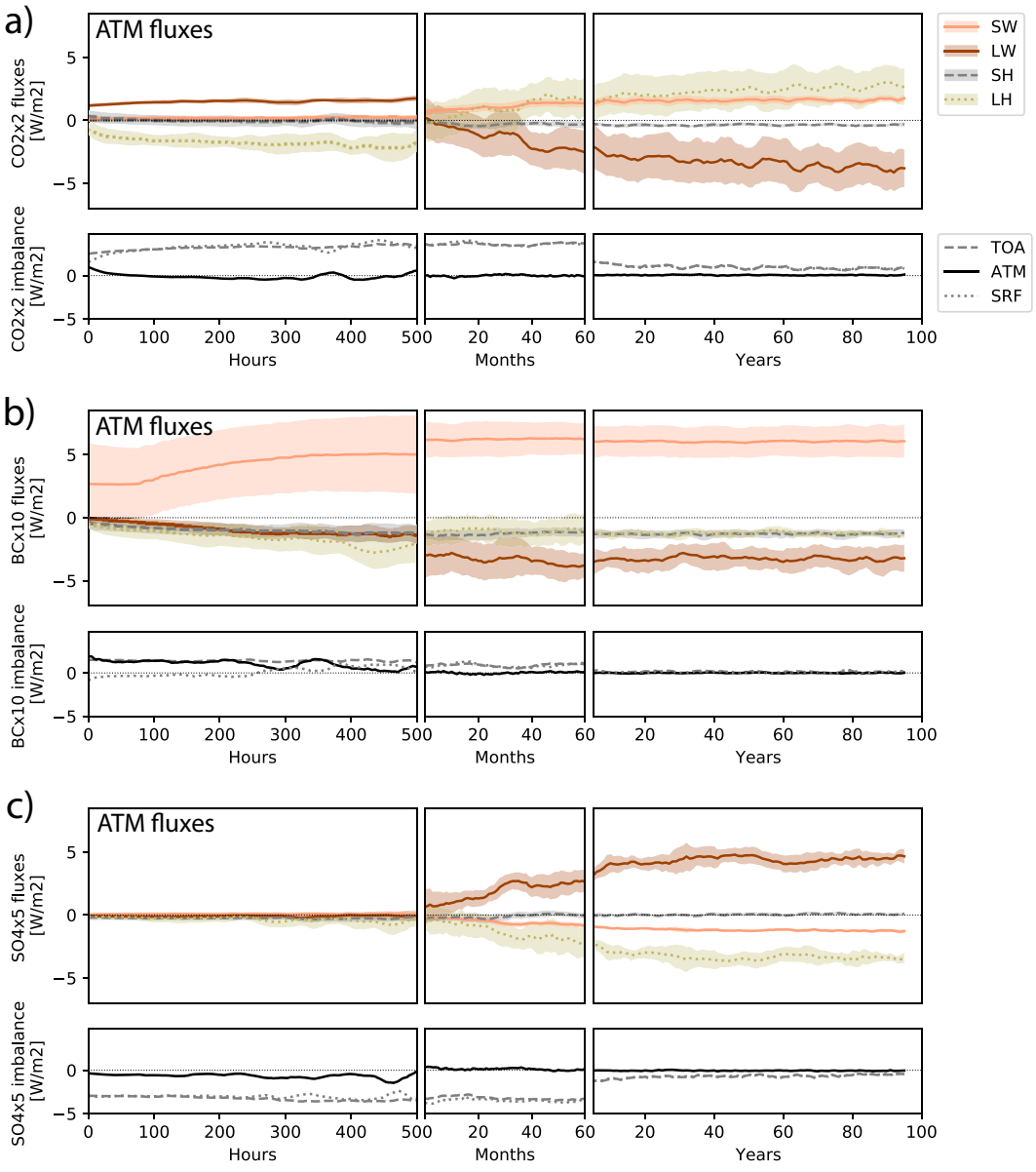

FIG. 2. Evolution of ATM radiative and energy fluxes (panels with colored lines) as well as evolution of TOA, ATM, and SRF radiative imbalance (panels with grayscale lines) for perturbations in (a) CO_2, (b) BC, and (c) SO_4. The imbalance is calculated as the sum of SW, LW, SH, and LH fluxes for different levels, so the ATM lines in the grayscale panels are the sum of all the ATM fluxes shown in colored panels. Individual radiative fluxes for TOA are not shown in Fig. S4. ATM is calculated as the difference between TOA and SRF fluxes. Lines show multimodel ensemble means and shading shows the model spread. Hourly panels are based on fixed-SST simulations, while monthly and yearly panels are based on fully coupled simulations.

After about 50 h (between 27 and 61 h for individual models; see Fig. S6 for radiative changes for individual models) the atmosphere reaches approximate equilibrium due to this CO_2-driven LH adjustment (Fig. 2a; narrow panels). At this time, the rapid precipitation response has levelled out (see Fig. 1c). After a couple of months, when the surface starts warming up, the higher temperatures cause more LW radiation to be emitted to space, which makes the atmospheric LW term change from positive to negative sign. Similarly, the long-term impact on evaporation (i.e., precipitation) also changes sign (Fig. 1c). This link between the evolution of the LW flux and the LH flux/precipitation can also be seen in the longer term, for instance, in a levelling out of all these terms after around 5–10 years for both CO_2 and SO_4.

For BC, the radiative response after just a few days is quantitatively similar to the full long-term response for all flux

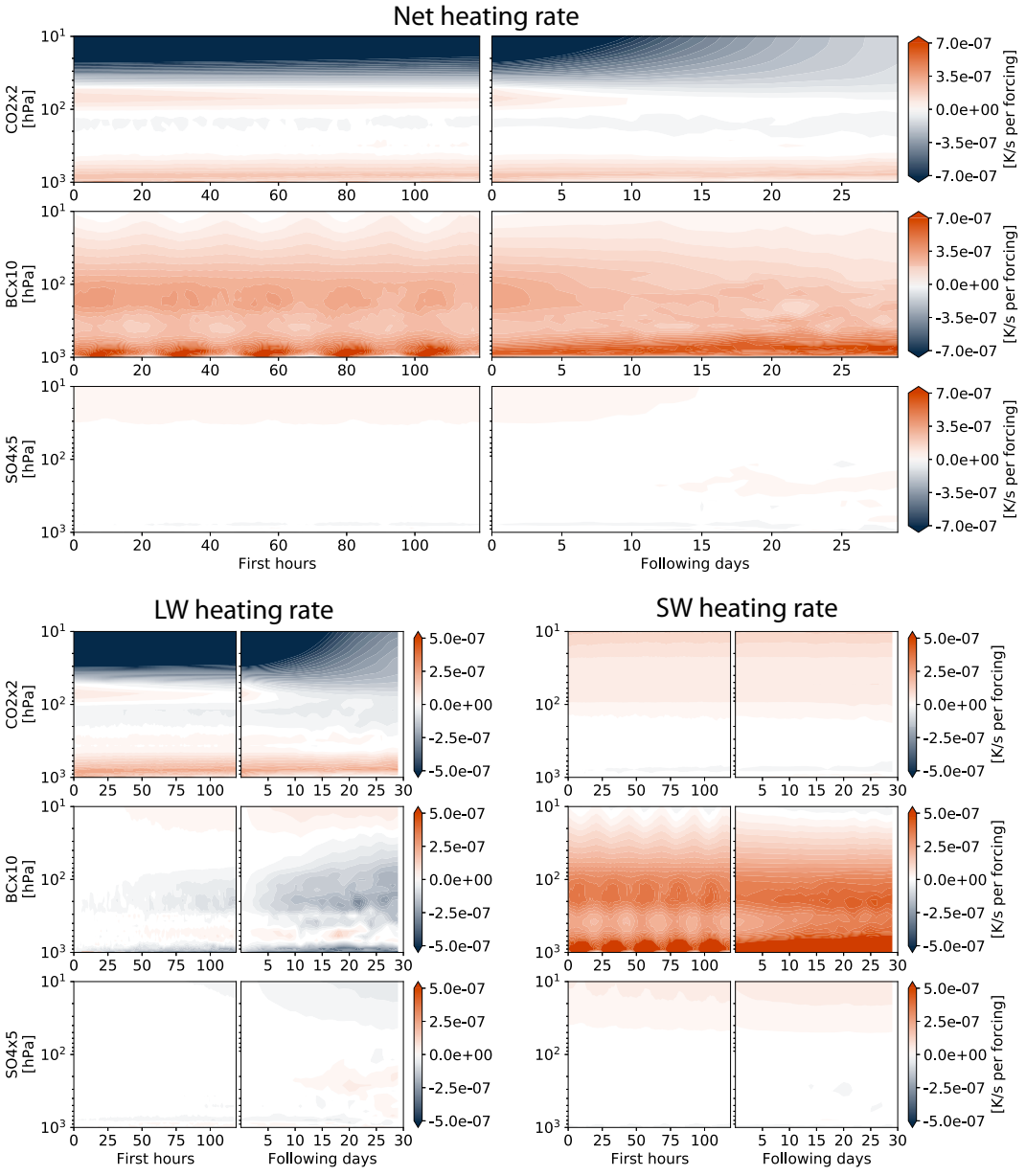

FIG. 3. (top) Evolution of global-mean profile of vertical net, (lower left) LW, and (lower right) SW heating rates for CO2x2, BCx10, and SO4x5. Leftmost panel in each panel pair shows changes for the initial hours, and rightmost panel shows subsequent daily values until 1 month after perturbation. All values are normalized by the absolute value of the ERF.

terms but LW, which takes longer to establish (Fig. 2b). There is an instant increase in the SW radiation term following the increased SW heating rate. Reemission from an increasingly heated up atmosphere causes a reduction in LW, which is very small for the first 100 h before the atmospheric warming really starts up (Fig. 3). In spite of the much weaker impact of BC on surface temperatures (compared to CO_2), the atmospheric absorption causes an increase in atmospheric stability and thus a reduction in latent heat flux comparable in both magnitude and time evolution to that from CO_2. The reduced sensible heat modulates the precipitation reduction from BC. The atmosphere is in energetic equilibrium after 2 weeks or around 300 h (Fig. 2b; narrow panels), after which the precipitation response has stabilized (Fig. 1c). There is a larger spread in the time scale for atmospheric equilibrium in BC (271–545 h) than in the CO_2 case, but the models that reach equilibrium fast (see, e.g., HadGEM3-GA4 in Fig. S6) have a precipitation change that stabilizes fast (Fig. S3) and vice versa.

For SO_4, the lack of an absorbing agent means that the instantaneous changes in the atmospheric radiative fluxes are

near zero—instead, changes are manifested in surface and top-of-atmosphere energy budgets. Sulfate aerosols are scatterers and interact strongly with solar radiation, but the solar energy that is hindered from reaching the surface is mostly scattered back to space, and hence the atmosphere experiences no significant change in radiative energy divergence (see, e.g., Tian et al. 2017). However, as the climate starts cooling, an increase in LW (more LW radiative energy remains in the atmosphere as less is emitted to space), a reduction in SW, and a reduction in LH create a pattern similar to but opposite in sign to that of CO_2, only without the change in sign in the first year (rapid and long-term responses mostly go in the same direction for SO_4).

b. *The instantaneous radiative response*

As shown in Fig. 2, radiative fluxes in the atmosphere system start responding to the change in a given atmospheric tracer immediately after a perturbation. In Fig. 3, we show the effect of this radiative impact on the net atmospheric heating rates for the first month (large upper set of panels). The net heating rate is the sum of LW and SW components (small lower set of panels).

Following the CO_2 perturbation is a strong instantaneous reduction in the net heating rate in the stratosphere. The SW heating rate is slightly positive, caused by the direct absorption of solar radiation by CO_2. The net effect, however, is dominated by the LW component. This, and the associated stratospheric cooling, is a well-known sign of CO_2 influence (e.g., Ackerman 1979; Wang and Huang 2020). The reduction in the LW heating rate starts diminishing after about 2 weeks as the stratosphere cooling establishes. We also see a lower-tropospheric (around 850 hPa) increase in heating rate, also driven by the LW component, which is caused by the enhanced absorption by CO_2 dominating any additional LW emission. Wang and Huang (2020) found in experiments with a one-dimensional radiation model that after about a month (which is how far our heating rate data go), stratospheric LW heating rates have diminished enough to be comparable in magnitude to the changes in the troposphere, and after 80 days, the stratospheric temperature adjustments are established and the LW stratospheric heating rates are down to almost zero (e.g., Hansen et al. 1997).

There is a strong similarity between all six models both in the magnitude and time scale of CO_2-induced heating rate changes (see individual model changes in Fig. S7). Interestingly, however, some of the models have a strong but temporary increase in the LW heating rate around 100 hPa (see Fig. S7 panels showing MIROC-SPRINTARS, HadGEM3-GA4, and ICON-HAM). Wang and Huang (2020) found a similar model inconsistency in this near-tropopause warming center in a range of CMIP5 models. Whereas previous studies (e.g., Lin et al. 2017) emphasize the longwave contribution to this warming, Wang and Huang (2020) found through dedicated experiments that the warming is critically dependent also on the shortwave effect.

Unlike for CO_2, the response to BC perturbation is dominated by the shortwave component, as BC particles are strong absorbers of solar radiation (Haywood and Shine 1995). This is clearly visible in the shortwave heating rate panel in Fig. 3, where near-surface BC causes clear diurnal cycles in the SW heating rate (visible in this global mean due to the predominant concentration at certain longitudes around 70°–120°E) fluctuating with the availability of sunlight. The BC absorption efficiency is strongest in the upper levels of the troposphere, where the aerosol absorption is enhanced by underlying layers of clouds and gases that reflect shortwave radiation and add to the absorption (Samset and Myhre 2011). For this reason, the shortwave heating rate for BC is strong in the upper troposphere where the efficiency of absorption is highest, as well as around the surface where concentrations are highest. Individual model heating rate responses to BC are shown in Fig. S8, and compared to CO_2, model responses to BC are more diverse. Much of this model diversity, however, is again due to the fact that MIROC-SPRINTARS and ICON-HAM perturbed BC emissions instead of concentrations. As it takes time for the aerosols to spread toward upper-atmospheric levels, in the first days, the aerosols only cause radiative influences closer to the surface in these models. In addition, Stjern et al. (2017) showed that GISS-E2.1 has significantly less BC near the surface (their Fig. 2) than CESM1-CAM4, NorESM1-M, MIROC-SPRINTARS, and HadGEM3-GA4 and more BC at higher altitudes. This can be recognized in model differences in the SW heating rates, which is focused around 100 hPa in GISS-E2.1 but is strongest near the surface in, e.g., NorESM1-M.

As seen in Fig. 3, BC causes a reduction in the LW heating rate in the stratosphere (around 100 hPa) already after a few hours. This is likely due to BC-induced warming in these levels. As shown in Fig. 4, the warming in this level is strong after a couple of weeks, causing further reduction in the LW heating rates (the Planck effect). In addition, in some models, reduced upwelling solar radiation reaching ozone in the middle and upper atmosphere (due to enhanced absorption by BC aerosols on the way up), further reduces LW emissions due to lowered ozone solar absorption, as also found in Stjern et al. (2017).

Perturbing scattering aerosols (SO_4) triggers changes in heating rates of similar magnitudes but opposing signs for the LW and SW components. The strongest change is the upper-level increase in the SW heating rate. Due to the upward scattering of SW radiation, ozone in the middle and upper atmosphere receives more SW radiation and thus a positive SW heating rate. The increase in temperature from this additional SW absorption causes a LW cooling in response (the local enhanced LW emission is not compensated for by increased LW absorption). The LW heating rates are further perturbed by cloud changes in the atmosphere, which will be discussed further in section 3d. The two emission-driven models, MIROC-SPRINTARS and ICON-HAM, have a much slower onset of the upper-level increase in the SW heating rate (Fig. S9 SW panels): while the SW heating rate is increased instantaneously in the concentration-driven models, it takes a couple of weeks to establish in the emission-driven models.

c. *ATM temperature responses*

While the first radiative response and, consequently, heating/cooling rates to perturbations in both greenhouse gases and

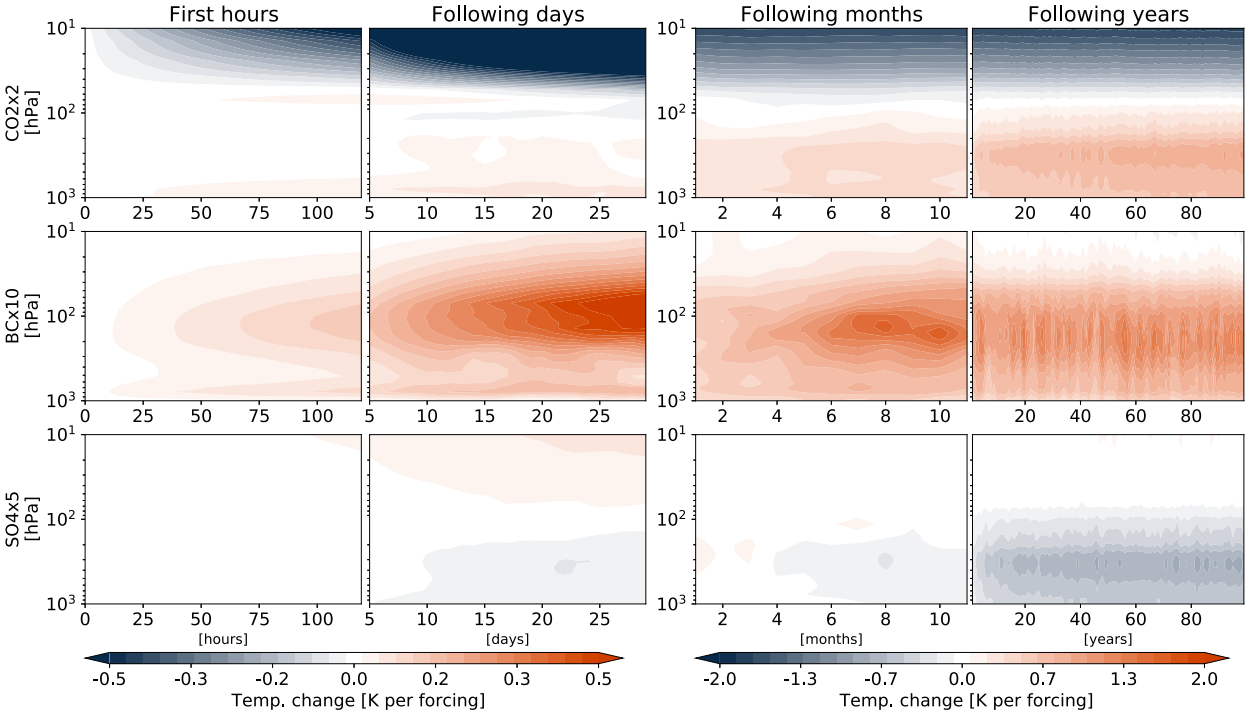

FIG. 4. Evolution of vertical global-mean temperature changes for (top) CO2x2, (middle) BCx10, and (bottom) SO4x5 for the initial hours and days (based on fixed-SST simulations) and then for the following months and years (based on fully coupled simulations). All values are normalized by the absolute value of the ERF.

aerosols are instantaneous, it takes a little more time for this to manifest as changes in atmospheric temperatures. In Fig. 4, we show vertical temperature changes on different time scales (as in Fig. 1a), where the first panel shows the first 120 h, and the next panels show changes for the subsequent days, months, and years, respectively. Figure S10 shows a version of Fig. 4 not normalized by ERF.

The stratospheric cooling following the CO_2 perturbation takes about a day to manifest as appreciable temperature changes. This is a robust time scale similar between all models (individual model temperature changes for CO_2 are shown in Fig. S11). Similarly, after about a day, we see a discernible lower tropospheric warming around 850 hPa, corresponding to the level with increased LW heating rate (Fig. 3). Increasing downwelling LW radiation contributes to the tropospheric heating, as does an increase in land surface temperatures (recall that even in fixed-SST mode, the models' land surface temperatures are allowed to evolve). While the stratospheric cooling gradually strengthens over the course of the first 2 weeks, at all times being stronger in the upper stratosphere (e.g., Fels et al. 1980; Manabe and Wetherald 1967), the tropospheric warming spreads upward from the surface. Consistent with our findings, Dong et al. (2009) found that after only 5 days, the pattern of the tropospheric temperature response to CO_2 was consistent with the equilibrium (fixed SST) value.

The BC-induced temperature change in the first days maximizes around 900 and 100 hPa. The LW heating rate (Fig. 3) and the atmospheric temperature change (Fig. 4) are interlinked through the Planck effect. However, after just a couple of months, the atmospheric heating is dominated by the upper-level heating. This underlines the importance of rapid adjustments other than those directly linked to the radiative changes. In the five models contributing to the PDRMIP study, the first monthly mean value of vertical transport shows upward transport of air at the model layer closest to the surface in all five models, which might indicate that the near-surface warming resulting from the strong positive near-surface warming rate is rapidly transported upward by convection, leaving the heating strongest at higher atmospheric levels. This is similar to the rapid convective adjustment noted by Wang and Huang (2020) following a doubling of CO_2. The emission-driven models, MIROC-SPRINTARS and ICON-HAM, show a definite lag compared to the other models in the BC perturbation, consistent with their delayed heating rate response. In spite of model differences in the early responses, the profiles of temperature changes are quite similar after a couple of years (Fig. S12).

Sulfate causes warming in the stratosphere as shortwave radiation scattered by the aerosols enhances SW absorption by the ozone layer, as explained in section 3b. The lower-level cooling, maximizing around 400 hPa in the global average, originates from a land surface cooling (as ocean temperatures are held fixed in these simulation setups) that follows as the scattering aerosols prevent some of the SW radiation from reaching the surface. In the first hours and days, the cooling is focused over land regions, in particular regions with high sulfate concentrations, but after a couple of weeks, the reduced sensible heat flux from surface to atmosphere has led to an

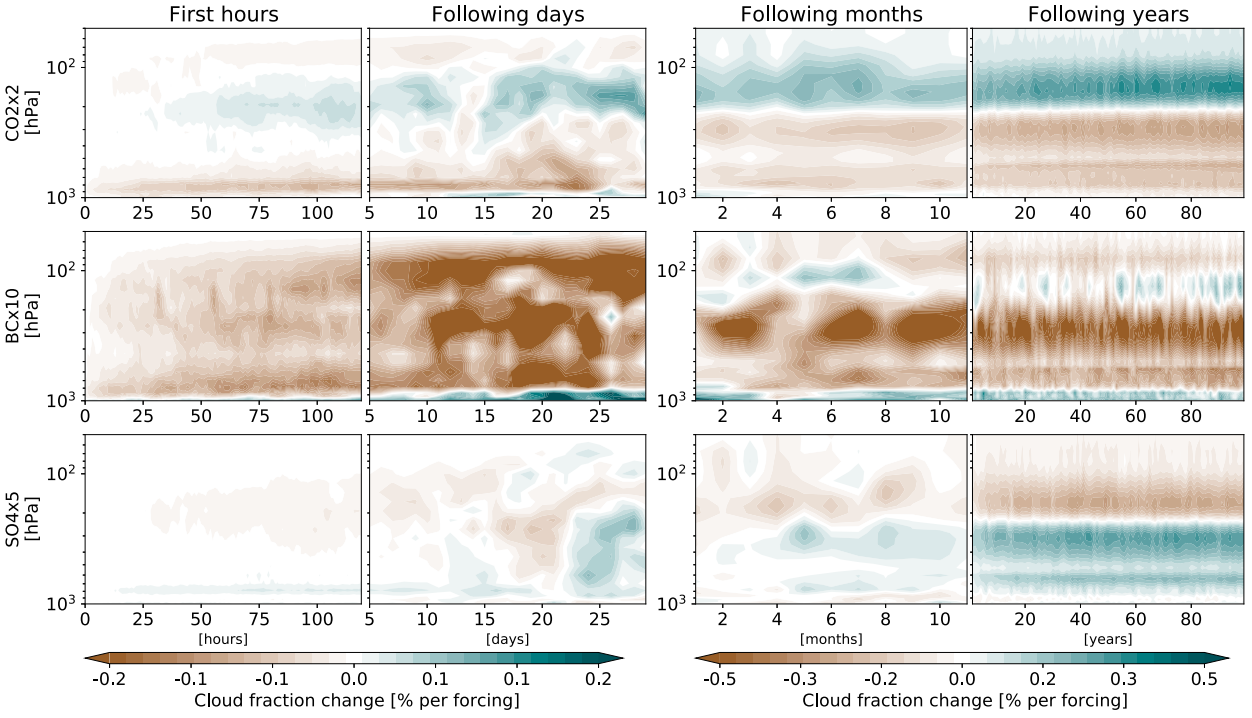

FIG. 5. As in Fig. 4, but for evolution of the vertical profile of global-mean cloud fraction changes (absolute percentage units) due to unit forcing from (top) CO_2, (middle) BC, and (bottom) SO_4. The multimodel ensemble average is shown.

atmospheric cooling seen over both land and ocean surfaces (not shown). The response to SO_4 is similar between the emission-driven and concentration-driven models after only a couple of weeks (Fig. S13), while the BC response is still far stronger in concentration-driven models after the first month.

d. Rapid and long-term changes to cloud cover

Rapid adjustments in the global-mean vertical cloud distribution are shown in Fig. 5 (with a nonnormalized equivalent in Fig. S14). Following an instantaneous doubling of CO_2, the clouds start responding after only a few hours. A clear reduction in low- to midlevel clouds (strongest around 850 hPa) is linked to a reduction in relative humidity (not shown), which occurs concurrently with enhanced heating rates and thus temperatures. Most likely, a combined effect of temperature-induced atmospheric stabilization and drying drives this reduction in low clouds. Note that the clouds start changing immediately after the temperatures. These rapid low-cloud reductions following a CO_2 perturbation in climate models are well documented (Colman and McAvaney 2011; Gregory and Webb 2008; Kamae and Watanabe 2013; Nam et al. 2018).

After a few more hours, we also see an increase in high clouds centered around 200 hPa. That CO_2 causes a rapid adjustment increase in high clouds has also been also shown before (e.g., Xu et al. 2020). Note that the increase in high clouds takes longer to establish and becomes particularly strong only after the stratospheric cooling has strengthened after a couple of weeks (Figs. 2, 3), indicating that this increase in high clouds might be convectively driven by the resulting increase in atmospheric instability at these altitudes. An increase in high clouds would also cool the upper troposphere at cloud top and heat the atmosphere below through longwave effects, which would further stabilize the profile. While the reduction in low clouds is almost solely driven by changes over ocean, the increase in high clouds is slightly stronger over land (not shown). All six models follow this same pattern of low-cloud reduction and high-cloud increase (Fig. S15). In a set of experiments using the MIROC5 model, Kamae and Watanabe (2013) found that the global-mean adjustments in short- and longwave cloud radiative effects are close to their equilibrium states within 2 days. Looking at the vertical patterns of cloud changes in Fig. 5, we see that the rapid response pattern is mostly established even before that for all three forcing agents.

After a couple of months (Fig. 5; monthly panel), a two-band pattern of CO_2-driven cloud reductions around 300 and 800 hPa is established. This pattern is seen in all models (Fig. S15). Looking at zonal-mean time-averaged cloud changes for the first year of fixed-SST versus coupled simulations (Fig. 6; upper row), we see that this cloud reduction at 300 hPa is not triggered until ocean temperatures are allowed to evolve, i.e., this part of the cloud-change pattern is a feedback response. Although the magnitude of these changes increases in the following year, the pattern does not change. The spatial correlation (calculated as Spearman's correlation, disregarding grid cells with less than 1% cloud fractions) is highly significant with a correlation coefficient of 0.78 between the 1-yr coupled and the full response. In other words, the pattern of the full-time cloud response is established after only a year.

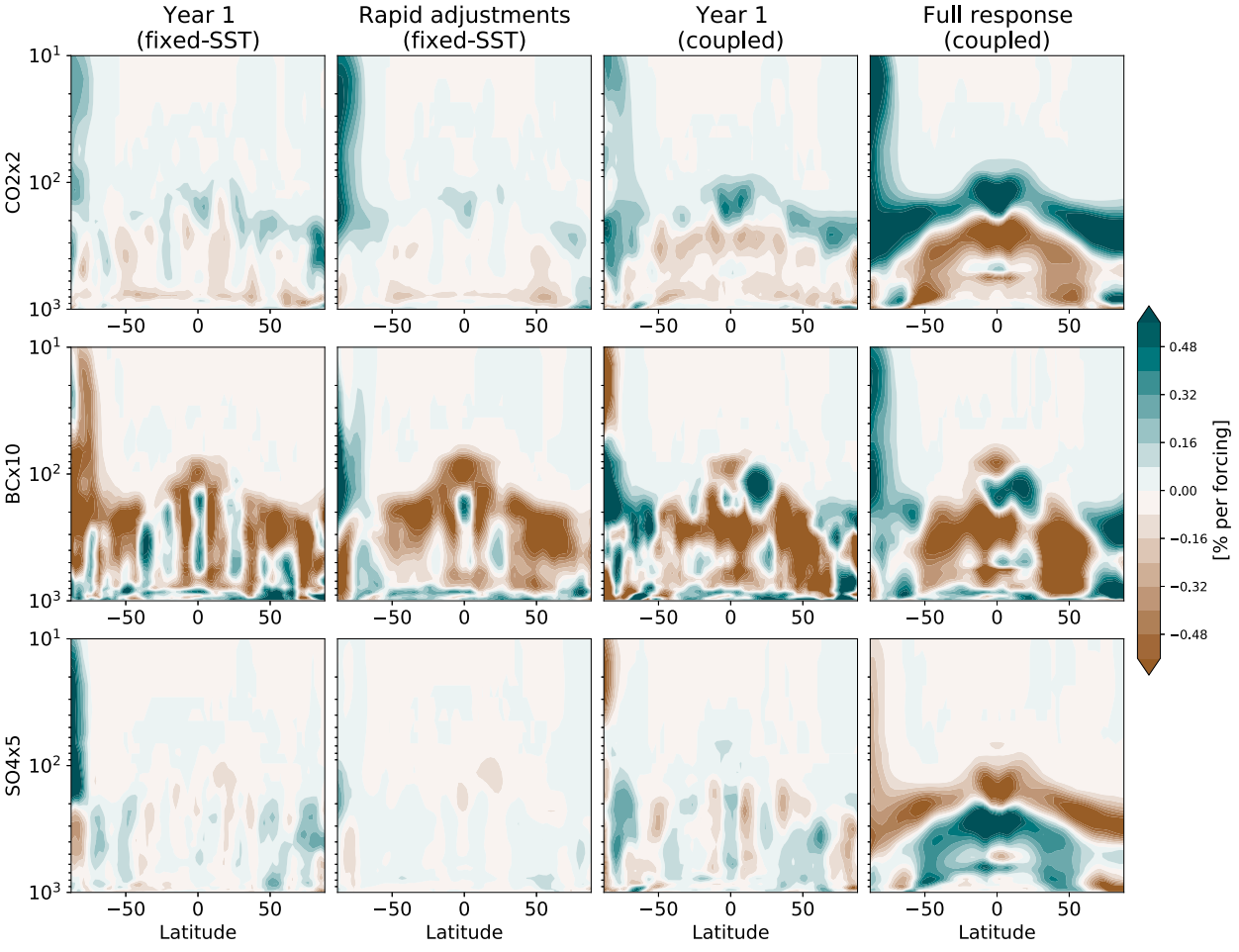

FIG. 6. Multimodel-average zonal–temporal-mean cloud fraction changes for (top) CO2x2, (middle) BCx10, and (bottom) SO4x5 for fixed-SST vs fully coupled simulations. The full response is defined as the average of years 50–100 of 100-yr fully coupled simulations, while rapid adjustments is defined as the average of years 6–15 of fixed-SST simulations. All values are normalized by the absolute value of the ERF.

Black carbon causes a general reduction in clouds at all vertical levels in the first few days of the simulation, at least in the global average. After almost 2 weeks, an increase in low clouds is established, the magnitude of which differs between the models (Fig. S16). The coupled simulations in the monthly and yearly panels of Fig. 5 show that the model-mean feedback response also includes a weak increase in the highest clouds. In an earlier PDRMIP study, Stjern et al. (2017) showed strong model agreement in the general cloud reduction from BC; most models had an increase in the very lowest clouds and a few models also showed an increase in the highest clouds. Similar model differences are also visible in Fig. S16. Here, we see that the increase in high (around 100 hPa) clouds, in the models that show this pattern, is not established until after a few of months. In general terms, however, the pattern of BC response is established after only a few days, and the magnitude of the response after less than half a year. Looking at the latitudinal-cloud-change distribution in Fig. 6, the correlation between the pattern of the 1-yr coupled and the full-time response is 0.66 and highly significant. Picking out, as an example, the midlatitude increases in midlevel clouds (40°–50°N; 380–180 hPa), 73% of the magnitude of this response is established after the first year. In comparison, for CO_2, only 19% of the magnitude of the prominent pattern of tropical high (200–100 hPa) cloud increase was established after 1 year.

The sulfate perturbation causes a relatively strong increase in clouds at the 800-hPa level after about one day (Fig. 5). As the temperature response is much slower in comparison (Fig. 4), these cloud changes may instead be microphysically driven, i.e., due to the aerosol–cloud interactions implemented in the GCMs. In an observationally based study of microphysical aerosol–cloud interactions in ship tracks, Gryspeerdt et al. (2021) find that the strongest change to cloud-droplet-number concentration occurs only 3 h after emission and that cloud adjustments continue to evolve further over a period of 10 h or more. Underlining the possibility of a microphysical influence is the fact that these processes can be parameterized very

differently between models and indeed the models disagree strongly on the initial cloud response in SO4x5 (Fig. S17), as opposed to what we find for CO_2 and BC. NorESM1-M even simulates a reduction in low clouds in the first couple of weeks. Like for CO_2, the zonal-mean pattern of the cloud responses is not well represented until feedback responses are included, and the monthly panel in Fig. 5 shows that SO_4 takes even longer than CO_2 for the vertical global-mean cloud change pattern to reach the full 100-yr pattern.

4. Conclusions

In this paper, we take a closer look at the time scales of the evolution of atmospheric changes that follow from idealized perturbations of CO_2, BC, and SO_4. Following the atmospheric processes as they evolve with time allows for an understanding of the underlying mechanisms. This cannot be achieved on the monthly mean data output typically investigated in global climate models.

In Fig. 7, we show a simplified summary of the findings in this analysis, illustrating the time evolution of a chosen set of responses (vertical temperature profiles and precipitation as well as changes to high and low clouds) to the three different climate forcers. The plot at the bottom shows how much of the "full climate response" (defined as the 100-yr fully coupled response) is realized at different time scales in terms of temperature and precipitation changes. Figure 7 shows that already within the first hours after a CO_2 perturbation, the stratospheric cooling has commenced and a subsequent increase in high clouds is seen. A reduction in low clouds is established even earlier due to increased longwave heating and a following warming and drying of the lower troposphere. The flux of latent heat goes down as a result of the longwave absorption by CO_2 in the atmosphere (helped by the physiological stomata effect represented in some models), stabilizing after about a month. This reduction in latent heat is followed by reduced precipitation, established within hours after the perturbation. As the climate and surface warms, we see a transition from decreasing to increasing latent heat flux and precipitation. The lowermost panel in Fig. 7, showing realized CO_2-driven precipitation change in dashed gray, clearly shows the transition from reduction to increase sometime in the first year of simulation. The warming also spurs a stronger increase in the high clouds—some of which is associated with an elevated tropical tropopause. Half of the global temperature change following the perturbation in CO_2 is realized after only 3 (model range 1–10) years, and after 10 years, the global-mean warming has realized more than 90% of its full response.

Perturbations of BC cause responses that in general are focused on the shorter time scales. The strong shortwave absorption by BC aerosols influences atmospheric heating rates, thus warming and stabilizing the troposphere (Fig. 7; vertical temperature profile). This atmospheric warming is observed after only a couple of hours and maximizes in about half a year (Fig. 4). The drying and stabilizing atmosphere spurns a general reduction in clouds at most levels, except the very lowest clouds, for which an increase is established after about a week. The maximum reduction in latent heat flux (and thus precipitation) is reached after about a month—see the bottom panel of Fig. 7, which shows a maximized precipitation response at the 1-month time scale. It should be noted, however, that 50% of the magnitude of the rapid precipitation adjustments (defined as the average response over years 6–15 in fixed-SST simulations) is realized within the first day for both CO_2 and BC. A notable exception is the two models that perturb aerosol emissions instead of concentrations—these models have rapid adjustments that are slower to establish. Intermodel differences also arise from differences in the vertical distribution of the aerosols, as seen in the different vertical profiles of radiative responses in GISS-E2.1 versus e.g., NorESM1-M.

Since the BC-induced precipitation response is a reduction at all time scales (Fig. 1b), we do not see a transition from positive to negative (as was seen for CO_2) in the bottom panel of Fig. 7. The effect of BC on surface temperature in the longer term is minor (see Fig. 1a and Stjern et al. 2017). Still, the impact of surface heating on precipitation can be seen as a reduction in the magnitude of the precipitation response in Fig. 7, which at 1 month is stronger (more than 100%) than the full response. As the climate warms (causing an increase in precipitation), the strong precipitation reduction is slightly muted. In the end, and unlike for CO_2, it is the rapid adjustments that dominate over the slower feedback effects in terms of magnitude.

Responses to changes in SO_4 aerosols differ from those to changes in BC aerosols in that they generally occur on longer time scales. The lack of an absorbing agent, present for both CO_2 and BC, makes for very weak climate responses in the first time scales. Still, the cooling of the global land surfaces, although slower than the warming caused by CO_2, commences relatively quickly and is visible (Fig. 1a) after just a few hours. For all drivers, the land warming in these fixed-SST runs set up a land–ocean temperature gradient that may spur rapid circulation changes not explored in this analysis. The largest model differences are found in the rapid (first month) responses in cloud cover following the perturbation of SO_4. Despite similar vertical and temporal responses in heating rates and temperature, cloud changes in the different models show substantial variation in their response to SO_4. This may be related to model differences in treatment of microphysical effects of SO_4. After about 2 years, the global-mean vertical cloud change patterns are similar between the models.

Previous analyses have shown intermodel variation in cloud responses stems to a larger extent from rapid adjustments than feedbacks. Here, we show that intermodel differences in cloud responses, while not large, are seen already in the first day after perturbation. It should be noted that much of the model differences in the aerosol experiments could have been reduced by using only concentration-driven models, as emission-driven models introduce a new set of choices and differences between the experiment setup and outcomes. The main features of the vertical and latitudinal pattern of the rapid cloud adjustments (for the BC perturbation also the magnitude) are established as soon as a few hours after idealized perturbations of CO_2, BC, and SO_4. This is true for all the six models.

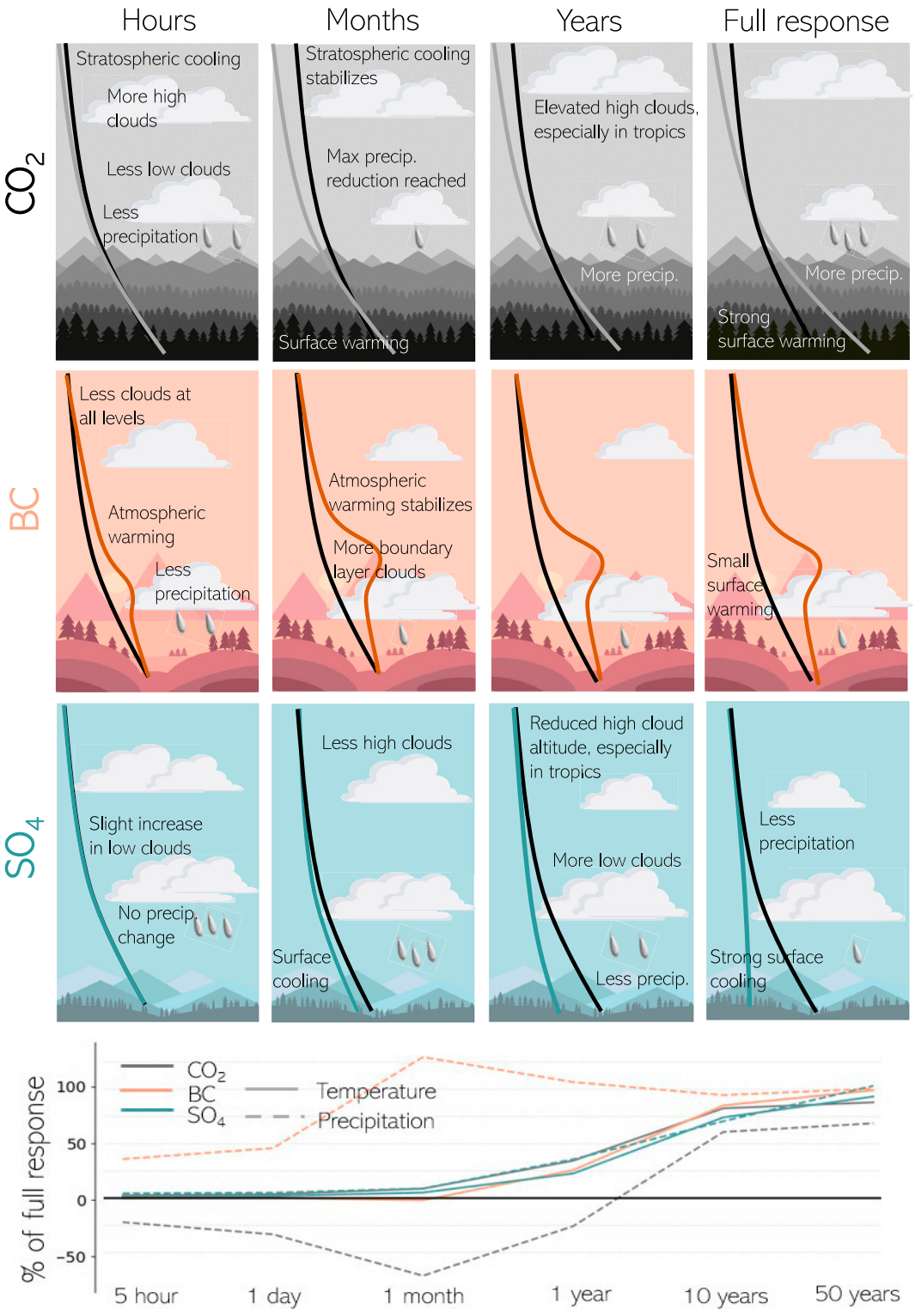

FIG. 7. Schematic of time scales of climate responses to CO_2, BC, and SO_4, focusing on the main changes to temperature, precipitation, and high and low clouds. Vertical lines illustrate changes from the baseline (black) vertical temperature profile. Note that temperature profiles are highly stylized, as are selected changes in high/low clouds and precipitation. (bottom) Model-average percentages at 100-yr (ERF normalized) response for chosen time periods.

Even given the noted differences, the six models do in general show surprisingly similar responses in both the magnitude and timing of change in heating rate, temperature, precipitation, and clouds. This underlines the robustness of model-simulated time scales and patterns of key climate responses to three of the most important climate drivers. The relevance of the difference in response time scales between these drivers becomes pertinent in the context of future emission changes. While focusing on short-lived climate drivers such as aerosols for achieving fast effects of mitigation efforts is well grounded, the rapid climate effects of CO_2 should not be forgotten. The climate impacts of CO_2 are indeed dominated by feedbacks and long time scales. The longevity of CO_2 in the atmosphere precludes any immediate reduction in CO_2 concentration. Yet, if we refrain from adding to this concentration—by lowering emissions or even by just keeping them constant—there will be a rapid response in clouds and precipitation as seen in Fig. 7. At constant concentration increase, the rapid adjustments are continuously realized. As concentrations cease to increase, these rapid adjustments to the increasing CO_2 are removed. We thus expect accordingly a certain increase in precipitation, increase in low clouds, and reduction in high clouds proportional to the CO_2 emissions decrease. For SO_4, which is quickly removed from the atmosphere but for which the response is dominated by the longer time scales, climate responses to mitigation efforts will be felt after a few months. And for BC, with its short atmospheric lifetime and dominance of short time scales, mitigation efforts are likely to have a fast impact on any detrimental climate effects that high emission regions are currently exposed to.

Acknowledgments. C. W. S., G. M., P. M. F., and J. Q. acknowledge funding by EU Horizon 2020 project CONSTRAIN (GA number 820829). H. J. and J. Q. further acknowledge support by the German Research Foundation (Joint call between National Science Foundation of China and Deutsche Forschungsgemeinschaft, DFG, GZ QU 311/28-1, project CloudTrend). M. S. has been supported by the Research Council of Norway [Grant 315195 (ACCEPT)]. C. D. W. was supported by the Natural Environment Research Council (Grant NE/L002515/1). T. T. was supported by the Environment Research and Technology Development Fund S-20 (JPMEERF21S12010) of the Environmental Restoration and Conservation Agency, Japan, the Japan Society for the Promotion of Science (JSPS) KAKENHI (JP19H05669), and the NEC SX supercomputer system of the National Institute for Environmental Studies, Japan. D. O. was supported by the Research Council of Norway (Grants 229771, 285003, and 285013) and by Notur/NorStore (NN2345K and NS2345K). The ICON-HAM model is developed by a consortium composed of ETH Zurich, the Center for Climate Systems Modeling (C2SM), Max Planck Institut für Meteorologie, Forschungszentrum Jülich, University of Oxford, the Finnish Meteorological Institute, and the Leibniz Institute for Tropospheric Research (TROPOS) and managed by TROPOS. The ICON model is developed in collaboration between MPI-M and the German Meteorological Service/Deutscher Wetterdienst (DWD) together with several partner institutes. J. Q. and H. J. would also like to thank Marc Salzmann, Leipzig University, for support with the ICON-HAM simulations. Simulations with HadGEM3-GA4 were performed using the Monsoon2 system, a collaborative facility supplied under the Joint Weather and Climate Research Programme, which is a strategic partnership between the Met Office and the Natural Environment Research Council. Data were stored and shared on project account NS9042KK on resources provided by UNINETT Sigma2—the National Infrastructure for High Performance Computing and Data Storage in Norway.

Data availability statement. All data are available upon request to the corresponding author.

REFERENCES

Ackerman, T. P., 1979: On the effect of CO_2 on atmospheric heating rates. *Tellus*, **31A**, 115–123, https://doi.org/10.3402/tellusa.v31i2.10416.

Allen, M. R., and W. J. Ingram, 2002: Constraints on future changes in climate and the hydrologic cycle. *Nature*, **419**, 224–232, https://doi.org/10.1038/nature01092.

Andrews, T., P. M. Forster, and J. M. Gregory, 2009: A surface energy perspective on climate change. *J. Climate*, **22**, 2557–2570, https://doi.org/10.1175/2008JCLI2759.1.

——, ——, O. Boucher, N. Bellouin, and A. Jones, 2010: Precipitation, radiative forcing and global temperature change. *Geophys. Res. Lett.*, **37**, L14701, https://doi.org/10.1029/2010GL043991.

Bellouin, N., and Coauthors, 2016: Regional and seasonal radiative forcing by perturbations to aerosol and ozone precursor emissions. *Atmos. Chem. Phys.*, **16**, 13 885–13 910, https://doi.org/10.5194/acp-16-13885-2016.

Bony, S., G. Bellon, D. Klocke, S. Sherwood, S. Fermepin, and S. Denvil, 2013: Robust direct effect of carbon dioxide on tropical circulation and regional precipitation. *Nat. Geosci.*, **6**, 447–451, https://doi.org/10.1038/ngeo1799.

Boucher, O., and Coauthors, 2013: Clouds and aerosols. *Climate Change 2013: The Physical Science Basis*, T. F. Stocker et al., Eds., Cambridge University Press, 571–657.

Cao, L., G. Bala, and K. Caldeira, 2012: Climate response to changes in atmospheric carbon dioxide and solar irradiance on the time scale of days to weeks. *Environ. Res. Lett.*, **7**, 034015, https://doi.org/10.1088/1748-9326/7/3/034015.

Colman, R. A., and B. J. McAvaney, 2011: On tropospheric adjustment to forcing and climate feedbacks. *Climate Dyn.*, **36**, 1649–1658, https://doi.org/10.1007/s00382-011-1067-4.

Deser, C., A. Phillips, V. Bourdette, and H. Teng, 2012: Uncertainty in climate change projections: The role of internal variability. *Climate Dyn.*, **38**, 527–546, https://doi.org/10.1007/s00382-010-0977-x.

Dong, B., J. M. Gregory, and R. T. Sutton, 2009: Understanding land–sea warming contrast in response to increasing greenhouse gases. Part I: Transient adjustment. *J. Climate*, **22**, 3079–3097, https://doi.org/10.1175/2009JCLI2652.1.

Doutriaux-Boucher, M., M. J. Webb, J. M. Gregory, and O. Boucher, 2009: Carbon dioxide induced stomatal closure increases radiative forcing via a rapid reduction in low cloud. *Geophys. Res. Lett.*, **36**, L02703, https://doi.org/10.1029/2008GL036273.

Fels, S. B., J. D. Mahlman, M. D. Schwarzkopf, and R. W. Sinclair, 1980: Stratospheric sensitivity to perturbations in ozone and carbon dioxide: Radiative and dynamical response. *J. Atmos. Sci.*, **37**, 2265–2297, https://doi.org/10.1175/1520-0469(1980)037<2265:SSTPIO>2.0.CO;2.

Forster, P., and Coauthors, 2016: Recommendations for diagnosing effective radiative forcing from climate models for CMIP6. *J. Geophys. Res. Atmos.*, **121**, 12 460–12 475, https://doi.org/10.1002/2016JD025320.

——, and Coauthors, 2021: The Earth's energy budget, climate feedbacks, and climate sensitivity. *Climate Change 2021: The Physical Science Basis*, V. Masson-Delmotte et al., Eds., Cambridge University Press, 923–1054.

Gregory, J., and M. Webb, 2008: Tropospheric adjustment induces a cloud component in CO_2 forcing. *J. Climate*, **21**, 58–71, https://doi.org/10.1175/2007JCLI1834.1.

Gryspeerdt, E., T. Goren, and T. W. P. Smith, 2021: Observing the timescales of aerosol–cloud interactions in snapshot satellite images. *Atmos. Chem. Phys.*, **21**, 6093–6109, https://doi.org/10.5194/acp-21-6093-2021.

Hansen, J., M. Sato, and R. Ruedy, 1997: Radiative forcing and climate response. *J. Geophys. Res.*, **102**, 6831–6864, https://doi.org/10.1029/96JD03436.

——, and Coauthors, 2005: Efficacy of climate forcings. *J. Geophys. Res.*, **110**, D18104, https://doi.org/10.1029/2005JD005776.

Haywood, J. M., and K. P. Shine, 1995: The effect of anthropogenic sulfate and soot aerosol on the clear sky planetary radiation budget. *Geophys. Res. Lett.*, **22**, 603–606, https://doi.org/10.1029/95GL00075.

Kamae, Y., and M. Watanabe, 2013: Tropospheric adjustment to increasing CO_2: Its timescale and the role of land–sea contrast. *Climate Dyn.*, **41**, 3007–3024, https://doi.org/10.1007/s00382-012-1555-1.

——, ——, T. Ogura, M. Yoshimori, and H. Shiogama, 2015: Rapid adjustments of cloud and hydrological cycle to increasing CO_2: A review. *Curr. Climate Change Rep.*, **1**, 103–113, https://doi.org/10.1007/s40641-015-0007-5.

Kvalevåg, M. M., B. H. Samset, and G. Myhre, 2013: Hydrological sensitivity to greenhouse gases and aerosols in a global climate model. *Geophys. Res. Lett.*, **40**, 1432–1438, https://doi.org/10.1002/grl.50318.

Lin, P., D. Paynter, Y. Ming, and V. Ramaswamy, 2017: Changes of the tropical tropopause layer under global warming. *J. Climate*, **30**, 1245–1258, https://doi.org/10.1175/JCLI-D-16-0457.1.

Lohmann, U., and Coauthors, 2010: Total aerosol effect: Radiative forcing or radiative flux perturbation? *Atmos. Chem. Phys.*, **10**, 3235–3246, https://doi.org/10.5194/acp-10-3235-2010.

Manabe, S., and R. T. Wetherald, 1967: Thermal equilibrium of the atmosphere with a given distribution of relative humidity. *J. Atmos. Sci.*, **24**, 241–259, https://doi.org/10.1175/1520-0469(1967)024<0241:TEOTAW>2.0.CO;2.

Myhre, G., and Coauthors, 2013: Anthropogenic and natural radiative forcing. *Climate Change 2013: The Physical Science Basis*, T. F. Stocker et al., Eds., Cambridge University Press, 659–740.

——, and Coauthors, 2017: PDRMIP: A Precipitation Driver and Response Model Intercomparison Project—Protocol and preliminary results. *Bull. Amer. Meteor. Soc.*, **98**, 1185–1198, https://doi.org/10.1175/BAMS-D-16-0019.1.

——, and Coauthors, 2018: Quantifying the importance of rapid adjustments for global precipitation changes. *Geophys. Res. Lett.*, **45**, 11 399–11 405, https://doi.org/10.1029/2018GL079474.

Nam, C., P. Kühne, M. Salzmann, and J. Quaas, 2018: A prospectus for constraining rapid cloud adjustments in general circulation models. *J. Adv. Model. Earth Syst.*, **10**, 2080–2094, https://doi.org/10.1029/2017MS001153.

O'Gorman, P. A., R. P. Allan, M. P. Byrne, and M. Previdi, 2012: Energetic constraints on precipitation under climate change. *Surv. Geophys.*, **33**, 585–608, https://doi.org/10.1007/s10712-011-9159-6.

Park, S.-W., J.-S. Kug, S.-Y. Jun, S.-J. Jeong, and J.-S. Kim, 2021: Role of cloud feedback in continental warming response to CO_2 physiological forcing. *J. Climate*, **34**, 8813–8828, https://doi.org/10.1175/JCLI-D-21-0025.1.

Richardson, T. B., and Coauthors, 2019: Efficacy of climate forcings in PDRMIP models. *J. Geophys. Res. Atmos.*, **124**, 12 824–12 844, https://doi.org/10.1029/2019JD030581.

Rotstayn, L. D., M. A. Collier, D. T. Shindell, and O. Boucher, 2015: Why does aerosol forcing control historical global-mean surface temperature change in CMIP5 models? *J. Climate*, **28**, 6608–6625, https://doi.org/10.1175/JCLI-D-14-00712.1.

Salzmann, M., 2016: Global warming without global mean precipitation increase? *Sci. Adv.*, **2**, e1501572, https://doi.org/10.1126/sciadv.1501572.

Samset, B. H., and G. Myhre, 2011: Vertical dependence of black carbon, sulphate and biomass burning aerosol radiative forcing. *Geophys. Res. Lett.*, **38**, L24802, https://doi.org/10.1029/2011GL049697.

——, and Coauthors, 2016: Fast and slow precipitation responses to individual climate forcers: A PDRMIP multimodel study. *Geophys. Res. Lett.*, **43**, 2782–2791, https://doi.org/10.1002/2016GL068064.

——, M. T. Lund, M. Bollasina, G. Myhre, and L. Wilcox, 2019: Emerging Asian aerosol patterns. *Nat. Geosci.*, **12**, 582–584, https://doi.org/10.1038/s41561-019-0424-5.

Sherwood, S. C., S. Bony, O. Boucher, C. Bretherton, P. M. Forster, J. M. Gregory, and B. Stevens, 2015: Adjustments in the forcing–feedback framework for understanding climate change. *Bull. Amer. Meteor. Soc.*, **96**, 217–228, https://doi.org/10.1175/BAMS-D-13-00167.1.

Smith, C. J., and Coauthors, 2020: Effective radiative forcing and adjustments in CMIP6 models. *Atmos. Chem. Phys.*, **20**, 9591–9618, https://doi.org/10.5194/acp-20-9591-2020.

Stjern, C. W., and Coauthors, 2016: Global and regional radiative forcing from 20% reductions in BC, OC and SO_4—An HTAP2 multi-model study. *Atmos. Chem. Phys.*, **16**, 13 579–13 599, https://doi.org/10.5194/acp-16-13579-2016.

——, and Coauthors, 2017: Rapid adjustments cause weak surface temperature response to increased black carbon concentrations. *J. Geophys. Res. Atmos.*, **122**, 11 462–11 481, https://doi.org/10.1002/2017JD027326.

Tian, D., W. Dong, D. Gong, Y. Guo, and S. Yang, 2017: Fast responses of climate system to carbon dioxide, aerosols and sulfate aerosols without the mediation of SST in the CMIP5. *Int. J. Climatol.*, **37**, 1156–1166, https://doi.org/10.1002/joc.4763.

Wang, Y., and Y. Huang, 2020: Understanding the atmospheric temperature adjustment to CO_2 perturbation at the process level. *J. Climate*, **33**, 787–803, https://doi.org/10.1175/JCLI-D-19-0032.1.

Williams, A. I. L., P. Stier, G. Dagan, and D. Watson-Parris, 2022: Strong control of effective radiative forcing by the spatial pattern of absorbing aerosol. *Nat. Climate Change*, **12**, 735–742, https://doi.org/10.1038/s41558-022-01415-4.

Xu, K.-M., Z. Li, A. Cheng, and Y. Hu, 2020: Changes in clouds and atmospheric circulation associated with rapid adjustment induced by increased atmospheric CO_2: A multiscale modeling framework study. *Climate Dyn.*, **55**, 277–293, https://doi.org/10.1007/s00382-018-4401-2.

Zelinka, M. D., S. A. Klein, K. E. Taylor, T. Andrews, M. J. Webb, J. M. Gregory, and P. M. Forster, 2013: Contributions of different cloud types to feedbacks and rapid adjustments in CMIP5. *J. Climate*, **26**, 5007–5027, https://doi.org/10.1175/JCLI-D-12-00555.1.